Composite Structures 255 (2021) 112968

Contents lists available at ScienceDirect

Composite Structures

journal homepage: www.elsevier.com/locate/compstruct

Nonlinear modeling of electro-aeroelastic dynamics of composite beams with piezoelectric coupling

Carlos R. dos Santos [a,*], Douglas R.Q. Pacheco [b], Haithem E. Taha [c], Mohamed Y. Zakaria [d]

[a] São Carlos School of Engineering - University of São Paulo (EESC/USP), São Carlos, SP, Brazil
[b] Institute of Applied Mathematics, Graz University of Technology, Graz 8010, Austria
[c] Department of Mechanical and Aerospace, University of California, Irvine, CA 92603, United States
[d] Aerospace Engineering Department, Military Technical College, Cairo 11766, Egypt

ARTICLE INFO

Keywords:
Energy harvesting
Aeroelasticity
Unsteady aerodynamics
Composite beam
Piezoelectricity

ABSTRACT

Structural and aerodynamic non-linearities can lead to persistent oscillations in aeroelastic systems, which allows the conversion of mechanical energy into electric power. Flexible beams represent an example of structures that can be used as energy harvesters. This work aims to model and analyze the non-linearities induced by the flow-structure interaction of an energy harvester consisting of a laminated beam integrated with a piezoelectric sensor. The cantilevered beam and the piezoelectric lamina are modeled using a nonlinear finite element approach, while unsteady aerodynamic effects are described by a state-space model that allows for arbitrary nonlinear lift characteristics. Wind tunnel tests for a fluttering beam in a broad range of flow speeds and preset angles of incidence were used to validate the electro-aeroelastic model. The matching of experimental and computational results reveals the importance of appropriately modeling structural and aerodynamic non-linearities for reproducing the physical electro-aeroelastic behavior of the system. These findings are of practical and theoretical relevance, and are further supported by the model's complete inability to reproduce experimental results when either of the non-linearities are "switched off".

1. Introduction

The interaction between fluids and structures may lead to interesting dynamic behaviors. In the case of bodies immersed in airflows, various aeroelastic phenomena can be observed – such as divergence, buffeting, flutter, galloping – depending on the characteristics of the structure under consideration and the flow conditions. The structural and aerodynamic non-linearities in such problems usually play a significant role in the response of the system, thereby enabling limit cycle oscillations, bifurcations or even chaotic motions [1]. In particular, the analysis of highly flexible wings has gained considerable attention in the aeroelastic community due to the increasing interest in high-altitude, long-endurance (HALE) aircraft where such wings are typically used. Previous studies demonstrated that the large displacements associated with these wings may significantly affect the aerodynamic loads, flutter speed and aeroelastic responses [2], potentially leading to limit cycle oscillations [3–5].

Much effort has been exerted towards exploiting persistent, stable limit cycle oscillations by converting their kinetic energy into usable electrical power. Energy harvesting schemes have recently been applied to several systems and the resulting harvested power may feed microelectromechanical systems or actuators [6]. As a matter of fact, the interest for harvesting energy from the environment has grown in the past decades and various solutions have been proposed for the development of harvesters [7–9]. In this sense, aeroelastic vibrations can also be employed for energy harvesting purposes. Galloping of prismatic structures [10] and vortex-induced vibrations of cylinders [11] have been addressed as possibilities for harvesting power from aeroelastic oscillations. Stable and persistent oscillations of airfoils beyond the flutter onset were also demonstrated by Marques et al. [9] as a possible option for energy harvesters. Similarly, the post-flutter behavior of plates has been investigated as a means to harvest power [12]. Zakaria et al. [13] experimentally quantified the power harvested from aeroelastic vibrations of a laminated beam during its post-flutter response. The beam was clamped perpendicularly to the airflow with a preset angle of incidence, and a piezoelectric lamina was employed for the conversion of kinetic energy into electric power. The harvester was able to generate energy when oscillating at a

* Corresponding author.
E-mail address: carlos.renan.santos@usp.br (C.R. dos Santos).

https://doi.org/10.1016/j.compstruct.2020.112968
Received 10 June 2020; Revised 15 July 2020; Accepted 10 September 2020
Available online 18 September 2020

specific frequency bandwidth constrained by structural and aerodynamic interactions.

From a modeling standpoint, there are basically two philosophies to tackle problems. The first is to use adopt a high-fidelity computational model such as the Navier–Stokes equations for the fluid flow and the equations of solid elasticity for the structure. However, the underlying computational burden is substantial and often ends up restricting the analysis to very few cases and flow conditions. The other philosophy relies on taking advantage of the special behavior of a certain system in particular conditions to develop a phenomenological reduced-order model. For instance, depending on load levels and dimensions, it may be possible to reduce three-dimensional solid models to shell, plate or beam models. This was done, for example, by Amini et al. [14], who used the Navier–Stokes equations for the flow field, but adopted the classic linear Euler–Bernoulli beam theory for the structure.

Also from the aerodynamic side there are several modeling possibilities. For low-speed laminar flows at low angles of incidence with respect to a slender body, linear potential theory is normally sufficient for predicting the main aerodynamic loads. For hypersonic and high-supersonic flows past plates or shells, piston theory has been successful for decades to account for aerodynamic forces [15,16], more recently in combination with piezoelectric excitation [17]. Exploiting the special aeroelastic behavior of flexible wings with high aspect ratio, Dunnmon et al. [18] and de Marqui Jr. et al. [19] analyzed energy harvesting from cantilevered beams attached to the trailing edge of airfoils, employing nonlinear modeling for structural dynamics and the unsteady vortex lattice method (UVLM) for the aerodynamics loads.

The approaches briefly mentioned above are only few of many methods that can circumvent the need for computing entire flow fields when one is interested only in the loads over the structure. While they typically yield a lower fidelity than continuum-based methods, they are capable of reproducing the main features of a coupled system's response, at a computational cost which is orders of magnitude lower. This is crucial in preliminary design stages where numerous design alternatives must be considered. In this context, a novel approach is presented here for modeling the energy harvesting of beams under low-speed aerodynamic loads. The appropriate modeling of such electro-aeroelastic behavior remains a somewhat open problem. In the present work, a finite element discretization of a nonlinear beam theory is coupled with a state-space model for the unsteady nonlinear aerodynamics to analyze the electro-aeroelastic behavior of cantilevered composite beams. Then, the theoretical predictions are compared to experimental measurements from the aeroelastic energy harvesting set up by Zakaria et al. [13]. The results reveal good agreement between model and experiments, and offer important insights into the role of structural and aerodynamic non-linearities in the electro-aeroelastic response. From a modeling perspective, this is the first time that the Kirchhoff flow model [20] is coupled to the state-space model proposed by Taha et al. [21]. Besides, another contribution of this work is bringing both structural and aerodynamic non-linearities together. Most efforts in the literature tend to focus on either source of nonlinearity, but seldom both. In fact, one of the main highlights in the present work is to show, through experimental validation, that both non-linearities must be considered if one wishes to accurately model and predict the electro-aeroelastic behavior of the system under consideration.

2. Structural model

The fluttering beam has a carbon-epoxy composite as a substrate and a piezoelectric layer attached to this substrate. As a consequence, the structural model needs to account for the different behavior associated with the composite substrate and the piezoelectric layer, as well as the electro-mechanical coupling of the piezoelectric.

2.1. Composite beam model

The Timoshenko model is used for the beam, thereby allowing for moderately large width-to-length ratios. In order to account for large vertical displacements w, the von Kármán strain-displacement relations are employed, namely,

$$\boldsymbol{\varepsilon} := \begin{Bmatrix} \varepsilon_x \\ \gamma_{xy} \\ \gamma_{xz} \end{Bmatrix} = \begin{Bmatrix} -z\frac{\partial\phi}{\partial x} + \frac{1}{2}\left(\frac{\partial w}{\partial x}\right)^2 \\ -z\frac{\partial\theta}{\partial x} \\ \frac{\partial w}{\partial x} - \phi + y\frac{\partial\theta}{\partial x} \end{Bmatrix}, \tag{1}$$

in which θ and ϕ are the torsion and bending angles, respectively. Direction z is upward vertical, and y is the airflow direction – both originating at the cross-sectional centroid, as indicated in Fig. 1. This geometrically nonlinear model accounts for large displacements but not for large strains, i.e., it assumes that the material still behaves in the linear elastic regime. Details on the material and kinematic modeling of laminated beams can be found in References [22,23].

2.2. Piezoelectric model

Similarly, the piezoelectric MFC is modeled as a Timoshenko beam eccentric to the main composite beam. Only axial strain due to bending is considered since rotational effects are assumed to be negligible near the beam root. It should be noted that the electric field also contributes to the material stresses on the piezoelectric MFC. Moreover, the electric field in the piezoelectric layer can be expressed as a function of the electric potential difference, v, between the top and the bottom of the layer. By assuming this variation to be linear, the electric field is then $-v/h_p$ and the axial stress in the piezoelectric is written as [24]

$$\sigma_{x_p} = c_{11}^E \varepsilon_{x_p} + c_{11}^E d_{31}\frac{v}{h_p} = c_{11}^E\left[(e-z)\frac{\partial\phi}{\partial x} + d_{31}\frac{v}{h_p}\right], \tag{2}$$

where c_{11}^E is the elastic modulus of the piezoceramic layer, d_{31} is the piezoelectric strain constant and e is the eccentricity between the piezoelectric and composite beam middle lines. From the constitutive equations of the piezoelectric, the electric displacement, D_z, is given by [24]:

$$D_z = c_{11}^E d_{31}\varepsilon_x - \varepsilon^{33}\frac{v}{h_p}, \tag{3}$$

where ε^{33} is the permittivity constant.

3. Aerodynamic model

The structural dynamics of the beam can be properly represented through the finite element model. On the other hand, aeroelastic analyses also require an appropriate modeling of the aerodynamic loads. For that goal, the state-space model for unsteady aerodynamics proposed by Taha et al. [21] offers an appropriate way to compute the

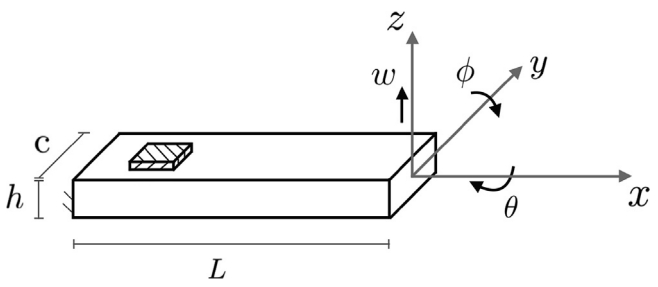

Fig. 1. Degrees of freedom of the composite beam.

aerodynamic loads during pitch and plunge excursions of each beam section.

3.1. State-space model for unsteady aerodynamics

Potential flow models for unsteady aerodynamics are very well known in the frequency domain due to the work of Theodorsen [25]. Other works also investigated the frequency response of airfoil aerodynamics [26,27]. On the other hand, by applying Duhamel's principle to the indicial lift response, also known as the Wagner response, Taha et al. [21] developed a state-space model for unsteady aerodynamics. The main advantage of the model of Taha et al. [21] in comparison to the previously developed state space models (e.g., by Leishman and his colleagues [28–31]) is its generalization of the Duhamel principle by considering the input to the potential flow lift dynamics to be the quasi-steady circulation (not the angle of attack or the airfoil normal velocity), relying on von Kármán and Sears' formulation [32]. By the applying the Duhamel superposition principle to the quasi-steady circulation as the aerodynamic input to Wagner's lift indicial response, the model of Taha et al. [21] allows arbitrary nonlinear steady lift curves, in contrast to the classical $2\pi \sin\alpha$ that is exclusively allowed in the previous state space models.

Given the quasi-steady circulation $\Gamma_{QS}(t)$, circulatory lift is written as [21]:

$$l_c(t) = \rho V_\infty[(1 - A_1 - A_2)\Gamma_{QS} + x_1 + x_2], \tag{4}$$

where ρ is the air density, V_∞ is the wind speed, and x_i $(i = 1, 2)$ are first-order aerodynamic states described by

$$\dot{x}_i(t) = \frac{2b_i V_\infty}{c}[-x_i(t) + A_i\Gamma_{QS}(t)], \tag{5}$$

with $A_1 = 0.165, A_2 = 0.335, b_1 = 0.0455$ and $b_2 = 0.3$ being the constants used for the Jones approximation of the Wagner function [33] and c is the chord length. Moreover, Γ_{QS} is defined as:

$$\Gamma_{QS}(t) = \frac{c}{2}V_\infty c_l(\alpha_{\text{eff}}(t)) + \pi\frac{c^2}{2}(0.5 - a)\dot{\theta}(t), \tag{6}$$

where a is the dimensionless distance between the elastic axis and the mid-chord and $c_l(\alpha_{\text{eff}}(t))$ is the two-dimensional static lift coefficient at the effective angle of attack $\alpha_{\text{eff}}(t)$. In the case where the beam undergoes pitch-plunge oscillations with an initial preset angle of incidence, $\alpha_{\text{eff}}(t) = \alpha_0 + \theta(t) - \tan^{-1}(\frac{\dot{w}}{V_\infty})$, with α_0 being the preset angle of incidence of the beam, θ is the structural rotation (twist angle) with respect to the equilibrium position and w is the vertical (bending) displacement of the beam.

On the other hand, the non-circulatory lift is computed by the relation given by Yan et al. [34]:

$$l_{nc}(t) = \pi\rho\frac{c^2}{4}\left[\dot{V}_\infty \sin\alpha - \ddot{w}\cos\alpha + (V_\infty\cos\alpha + \dot{w}\sin\alpha)\dot{\alpha} - a\frac{c}{2}\ddot{\alpha}\right], \tag{7}$$

where $\alpha(t) = \alpha_0 + \theta(t)$ is the local geometric angle of attack, which differs from the effective angle of attack $\alpha_{\text{eff}}(t) = \alpha(t) - \tan^{-1}(\frac{\dot{w}}{V_\infty})$; the latter accounts for plunging effects. Similarly, the non-circulatory moment at the elastic axis is written as [34]:

$$m_{nc}(t) = \pi\rho\frac{c^2}{4}\left[\frac{1}{2}(V_\infty^2 - \dot{w}^2)\sin 2\alpha - V_\infty\dot{w}\cos 2\alpha + a\frac{c}{2}(\dot{V}_\infty\sin\alpha - \ddot{w}\cos\alpha) - \left(\frac{1}{8} + a^2\right)\left(\frac{c}{2}\right)^2\ddot{\alpha}\right], \tag{8}$$

and the circulatory component of moment at the elastic axis is given by [35]:

$$m_c(t) = \pi\rho\frac{c^2}{4}V_\infty\left[\dot{w}\cos\alpha - V_\infty\sin\alpha - \frac{c}{2}\left(\frac{1}{2} - a\right)\dot{\alpha}\right] + m_f, \tag{9}$$

where m_f is the moment caused by the circulatory lift considering the distance between the elastic axis and the aerodynamic center at the quarter chord. In the potential flow theory $m_f = (1/4 + a/2)l_c(t)c$. However, in the analyses of this work, effects of flow separation may be taken into account due to the occurrence of moderately high angles of attack.

3.2. Nonlinear model for separated flows

The unsteady state space model of Taha et al. [21], described above, requires a prior knowledge of the steady lift curve. Here, the classical potential flow relation $c_l = 2\pi\sin\alpha$ is not assumed. Rather, the Kirchhoff nonlinear aerodynamic model for separated flows [36] is adopted. Using such a model, Thwaites [20] showed that the nonlinear lift coefficient of a flat plate at angle of attack α is given by $c_l(\alpha) = 0.25c_l^p(\alpha)\left(1 + \sqrt{f}\right)^2$, where c_l^p is the attached-flow lift coefficient and f is the chord-normalized location of the separation point. That is, for an attached flow, $f = 1$; hence, $c_l = c_l^p$. Typically, the attached flow lift coefficient is taken as $c_l^p = 2\pi\sin\alpha$. However, this relation results in a lift coefficient that is maximum at $\alpha = 90°$, which is not physically plausible. Rather, we use the formula proposed by Wang et al. [37]: $c_l^p = \pi\sin 2\alpha$. As such, we write the steady nonlinear lift characteristics as

$$c_l(\alpha) = \pi\sin(2\alpha)\left(\frac{1 + \sqrt{f}}{2}\right)^2. \tag{10}$$

In addition, the Beddoes–Leishman (BL) model [38] offers a suitable empirical representation for $f(\alpha)$, that is:

$$f(\alpha) = \begin{cases} 1 - 0.3e^{\frac{|\alpha| - \alpha_1}{s_1}} & \text{if } |\alpha| \leqslant \alpha_1 \\ 0.04 + 0.66e^{\frac{\alpha_1 - |\alpha|}{s_2}} & \text{if } |\alpha| > \alpha_1 \end{cases}, \tag{11}$$

where α_1, s_1 and s_2 are empirical constants to be determined from the static lift curve as a function of the angle of attack.

As for the aerodynamic moment, the BL model [38] proposed the use of an empirical relation between the static normal force and the moment m_f at the quarter chord accounting for flow separation, which is extended here by using the lift coefficient without loss of accuracy, according to:

$$\frac{m_f}{l_c c}(\alpha) = K_0 + K_1(1 - f) + K_2\sin(\pi f^2) + \left(\frac{1}{4} + \frac{a}{2}\right), \tag{12}$$

where K_0, K_1 and K_2 are constants to be determined from the static curve of moment at the quarter chord as a function of the angle of attack. The value of m_f is applied in Eq. (9).

For a flat plate at $Re \approx 10^4$ and thickness around 1% of the chord length, such as in the current experiment, Okamoto et al. [39] measured the lift coefficient for angles of attack up to 20°, as shown in Fig. 2(a). Under similar conditions, Amandolese et al. [40] assessed the moment coefficient about the mid-chord of a flat plate, $c_{m_{ea}}$, as presented in Fig. 2(b). These curves allowed the calibration of the semi-empirical parameters in Eqs. (11) and (12), as illustrated in Fig. 2. The resulting steady lift characteristics (10) is then used to determine the quasi-steady circulation according to (6), which is then fed to the state space model (4) and (5) to determine the circulatory lift l_c. Finally, the total lift and moment per beam section are given, respectively, by: $l = l_c + l_{nc}$ and $m = m_c + m_{nc}$.

4. Discretization and solution

4.1. Principle of virtual work

The coupling of aerodynamics with the electro-structural system is done via the Principal of Virtual Work (PVW). It states that the virtual work due to external forces must be fully converted into the variation of the system's virtual internal energy, for any compatible virtual

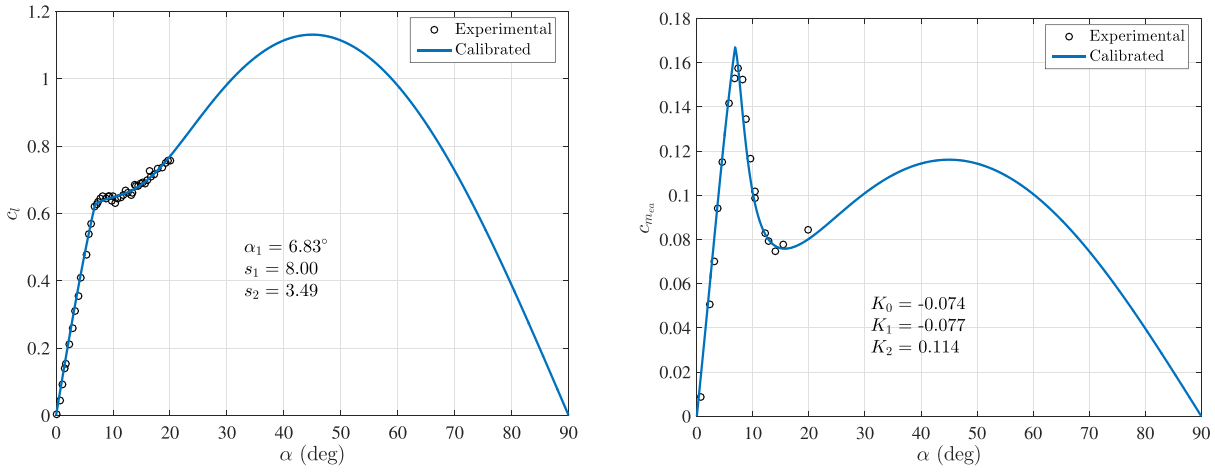

(a) Lift coefficient (b) Moment coefficient at the elastic axis

Fig. 2. Calibration of parameters for the Beddoes–Leishman model for a flat plate at $Re \approx 10^4$. Experimental lift from Okamoto et al. [39] and moment coefficient from Amandolese et al. [40].

displacement field. For the aeroelastic problem (no piezoelectricity), this balance can be written as

$$\int_\Omega \left[\rho_s\left(\ddot{w}\delta w + z^2\ddot{\theta}\delta\theta + y^2\ddot{\phi}\delta\phi\right) + \delta\boldsymbol{\varepsilon}\mathbf{C}\boldsymbol{\varepsilon}\right]\mathrm{d}\Omega = \int_0^L l\delta w + m\delta\theta \ \mathrm{d}x, \tag{13}$$

in which δ represents virtual quantities, Ω is the beam's domain, L is its length, $\mathbf{C}$ is the laminate's constitutive matrix [22,23] and (l, m) are the aerodynamic forces (total lift and moment). When there is one or more piezoelectric laminae, the virtual energy due to the additional components can be simply added to the left-hand side of Eq. (13).

4.2. Spatial discretization

The spatial discretization is done using standard first-order Lagrangian finite elements. Using the same finite element interpolants for the virtual and real displacements in the PVW and enforcing the principle for every compatible virtual field yields the nonlinear ODE system

$$\begin{cases} \mathbf{M}\ddot{\mathbf{U}} + [\mathbf{K}_0 + \mathbf{H}(\mathbf{U})]\mathbf{U} - \Theta v = \mathbf{F}(\mathbf{U}, \dot{\mathbf{U}}, \ddot{\mathbf{U}}), \\ C_p\dot{v} + \frac{v}{R} + \Theta^T\dot{\mathbf{U}} = 0, \end{cases} \tag{14}$$

where $\mathbf{U}$ is the vector of nodal degrees of freedom (DOFs), $\mathbf{F}$ is the aerodynamic force vector, $\mathbf{M}$ is the mass matrix, and $\mathbf{K}_0$ and $\mathbf{H}$ are the stiffness matrices coming from the linear and nonlinear structural contributions, respectively (details on the construction of the finite element matrices can be found in References [41,42]). Note that the second equation corresponds to the electrodynamics of the piezoelectric sensor. The electro-mechanical coupling matrix is denoted by Θ, R is the external load resistance and C_p is the piezoelectric capacitance. More details on the matrices related to the piezoelectric discretization can be found in Reference [43].

4.3. Temporal discretization

A Newmark-type scheme is used for integrating the nonlinear ODE system (14) in time. The solution $\mathbf{U}_{n+1}^{(k+1)}$ at the $(k+1)$-th iteration of the $(n+1)$-th time step is found by solving [44]

$$\hat{\mathbf{K}}\mathbf{U}_{n+1}^{(k+1)} = \hat{\mathbf{F}}_{n+1}^{(k)} - \frac{\Delta t^2}{4}\left[\mathbf{H}\left(\mathbf{U}_{n+1}^{(k)}\right)\right]\mathbf{U}_{n+1}^{(k)}, \tag{15}$$

where

$$\hat{\mathbf{F}}_{n+1}^{(k)} = \frac{\Delta t^2}{4}\tilde{\mathbf{F}}\left(\mathbf{U}_{n+1}^{(k)}, \dot{\mathbf{U}}_{n+1}^{(k)}, \ddot{\mathbf{U}}_{n+1}^{(k)},\right) + \tilde{\mathbf{M}}\left[\mathbf{U}_n + \Delta t\dot{\mathbf{U}}_n + \frac{\Delta t^2}{4}\ddot{\mathbf{U}}_n\right] + \tilde{\mathbf{G}}\left[\frac{\Delta t}{2}\mathbf{U}_n + \frac{\Delta t^2}{4}\dot{\mathbf{U}}_n\right], \tag{16}$$

and

$$\hat{\mathbf{K}} = \tilde{\mathbf{M}} + \frac{\Delta t}{2}\tilde{\mathbf{G}} + \frac{\Delta t^2}{4}\tilde{\mathbf{K}}, \tag{17}$$

where

$$\tilde{\mathbf{M}} = \begin{bmatrix} \mathbf{M} & \mathbf{0} \\ \mathbf{0} & 0 \end{bmatrix}, \quad \tilde{\mathbf{G}} = \begin{bmatrix} \mathbf{0} & \mathbf{0} \\ \Theta^T & C_p \end{bmatrix}, \quad \tilde{\mathbf{K}} = \begin{bmatrix} \mathbf{K}_0 & -\Theta \\ \mathbf{0} & 1/R \end{bmatrix}, \quad \tilde{\mathbf{F}} = \begin{bmatrix} \mathbf{F} \\ 0 \end{bmatrix}. \tag{18}$$

When the iterations reach the desired convergence, the velocity and acceleration vectors are updated as

$$\dot{\mathbf{U}}_{n+1} = -\dot{\mathbf{U}}_n + \frac{2}{\Delta t}(\mathbf{U}_{n+1} - \mathbf{U}_n), \tag{19}$$

$$\ddot{\mathbf{U}}_{n+1} = -\ddot{\mathbf{U}}_n + \frac{4}{\Delta t^2}\left(\mathbf{U}_{n+1} - \mathbf{U}_n - \Delta t\dot{\mathbf{U}}_n\right). \tag{20}$$

A schematic of the whole computational model is presented in Fig. 3. As for the PVW, aerodynamic loads contribute to the virtual external work. The computation of these loads start with the assessment of $f(\alpha)$ according to the BL model, which is applied to the calculation of the static lift coefficient considering separation effects. This static lift and the local kinematics define the quasi-steady circulation that is input for the state-space model proposed by Taha et al. [21]. The state-space model delivers the circulatory lift, also input for the circulatory moment at each beam section. Non-circulatory loads depend on the local kinematics only and their sum with circulatory quantities give the total lift and moment per beam section. On the other side, the virtual internal work depends on the laminate's constitutive matrix, which comes from the stress–strain relations obtained through the Timoshenko beam theory considering piezoelectricity, the laminate theory and the von Kármán strain. The equivalence between external and internal virtual works discretized through the finite element method results in differential equations that are numerically integrated by Newmark's method.

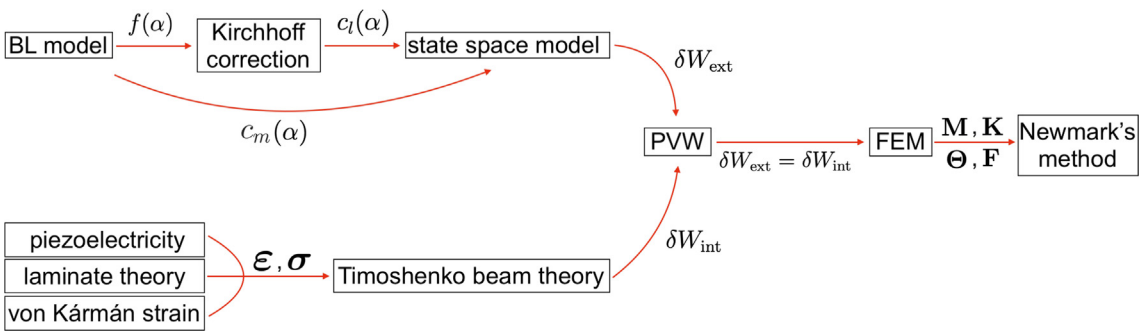

Fig. 3. Schematic of the computational model.

5. Experimental setup

A composite beam was fabricated and exposed to the airflow of a suction-type wind tunnel with an open circuit. The composite beam was manufactured with three layers of plain weave SGP196 (IM7-GP) carbon fiber fabric organized as 90°. Two thermoset polymers were employed for the matrix: the PR 2032 (resin), and the PH3665 (hardener). A piezoelectric macro-fiber composite (MFC) was attached to the beam 5 mm below the fixed end. The output voltage of the MFC was acquired at a rate of 2000 Hz. A resistor box was connected to the output wire of the MFC and the effects in the harvested power of different electrical loads were analyzed. Important parameters of the composite beam and of the piezoelectric MFC are depicted in Table 1, such as previously measured by Zakaria et al. [13].

The beam was attached at the roof of the test chamber to a stepper motor that sets a specific angle of incidence α_0 between the chord and the airflow. The test chamber had a cross section of 520 × 520 mm. The tests were performed by varying the wind speed and the angle α_0 with the aid of a stepper motor. Fig. 4 shows the experimental setup.

Limit cycle oscillations were observed for wind speeds beyond 7 m/s and energy was harvested through the piezoelectric layer. Fig. 5 shows the peaks and valleys of the output voltage that was harvested during the stable oscillations considering two different preset angles for the initial incidence of the beam with respect to the free-stream velocity and a resistance $R = 10^6\ \Omega$.

6. Results

The structural modes and natural frequencies can be computed from the linear matrices of the finite element method. The beam was

Table 1
Beam and piezoelectric properties [13].

	Parameter	Symbol	Value (unit)
Beam	Density	ρ	1550 (kg/m^3)
	Length	L	260 (mm)
	Thickness	h	0.49 (mm)
	Chord	c	20 (mm)
	Tensile moduli	E_{11}	29 (GPa)
		E_{22}	2.9 (GPa)
	Poison's ratio	ν_{12}	0.332
	Shear moduli	G_{12}	1.69 (GPa)
		G_{13}	1.69 (GPa)
		G_{23}	1.27 (GPa)
Piezoelectric	Density	ρ_p	7800 (kg/m^3)
	Piezoelectric constant	d_{31}	−190 (Pm/V)
	Strain permittivity	ε^{33}	15.9 (nF/m)
	Active length	L_p	40 (mm)
	Active width	c_p	10 (mm)
	Thickness	h_p	0.26 (mm)
	Young's modulus	E_p	66 (Gpa)

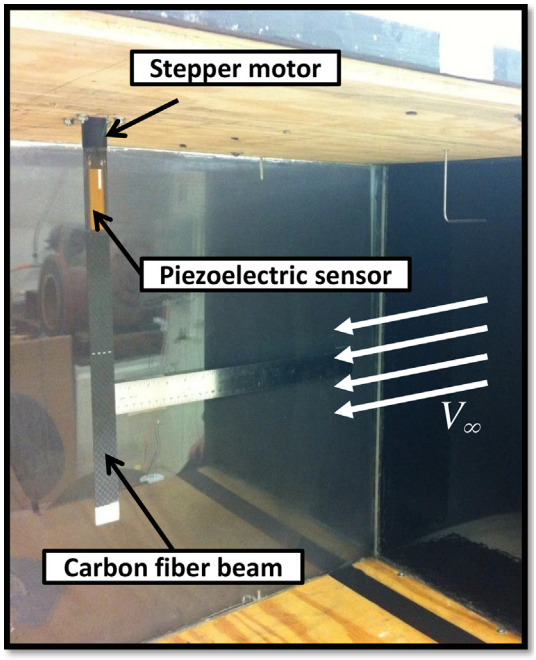

Fig. 4. Cantilevered beam as set in the center of the roof of the test section [13].

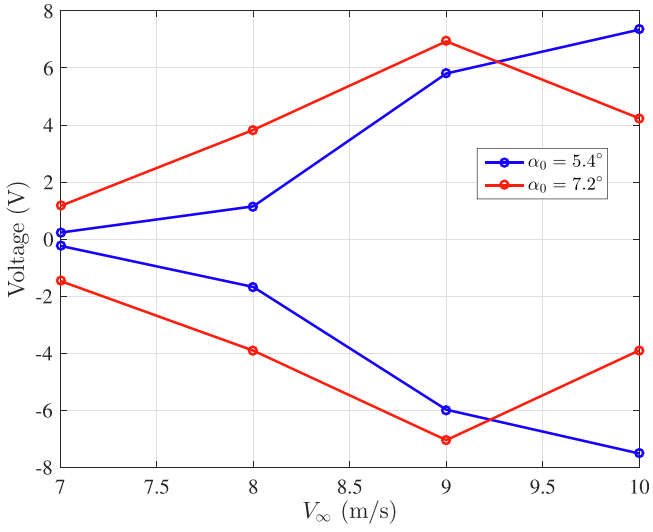

Fig. 5. Maximum and minimum values of the output voltage measured experimentally.

discretized with 65 elements, in the following way: 5 elements from the root to the beginning of the piezoelectric, 10 elements along the piezoelectric region and 50 elements in the remaining length. Considering a mesh with 10 times more elements, the maximum difference in the natural frequency was 0.07%, in the second bending mode. Therefore, the selected grid with 65 elements is already converged for aeroelastic analyses. In the case with an open circuit, the natural frequencies are compared to those experimentally measured, as in Fig. 6. The maximum difference between computational and experimental results is observed for the second bending mode, where the computational method predicts a natural frequency 5.8% lower than the experimental value. This small difference between computational and experimental results is most likely associated with imperfections in manufacturing and idealizations in modeling. In this sense, the alignment of the plies, the distribution of epoxy along the beam, the variation of temperature throughout the curing time, among others, are sources of imprecision in the final product. Therefore, the structural modeling of the composite beam with the piezoelectric device is in accordance with the experimental measurements. Moreover, no torsion is observed in the bending modes and the structural torsion of the first torsional mode in the piezoelectric region is only 3.6% of the maximum torsional angle, which is observed at the beam tip. In addition, the relative torsion between the extremities of the piezoelectric is only 0.03% of the tip torsion. Therefore, the assumption that torsional effects are negligible to the energy harvesting is valid in the case of interest.

From the aerodynamic point of view, the function $c_l(\alpha_{\text{eff}}(t))$ in Eq. (6) is able to account for any non-linearity in the lift coefficient as a function of the angle of attack. However, a first logical essay to the aerodynamic model is the case when $c_l(\alpha_{\text{eff}}(t)) = 2\pi\alpha_{\text{eff}}(t)$, which recovers the classical unsteady potential flow theory. In this case, as shown in Fig. 7 for $V_\infty = 8$ m/s and $\alpha_0 = 5.4^\circ$, the oscillations are damped and an equilibrium position is reached by the beam. Such a behavior is observed whether considering the linear or the complete nonlinear beam model. These results are not in accordance with experimental observations because limit cycle oscillations were expected under the same conditions, as indicated in Fig. 5. Since the structural dynamics were previously captured with good accuracy, the impossibility of matching experimental results must be associated with the unsteady aerodynamic model. Other efforts also pointed the limitation of the classical unsteady potential flow theory on predicting the flutter onset in some cases [45,46] due to the controversial unsteady Kutta condition (see the recent article by Taha and Rezaei [47] for a detailed discussion on the topic and a viscous extension of the theory that corrects for the Kutta's lift). Besides, Fig. 7(b) suggests that high angles of attack may be attained during the beam motion, thereby indicating the need for an aerodynamic model that is able to capture aerodynamic effects at high angles of attack, such as the flow separation. Furthermore, Fig. 7(a) illustrates the importance of using the complete nonlinear structural model since the linear model predicts an extremely high tip displacement that violates the hypothesis of low displacements adopted on its formulation.

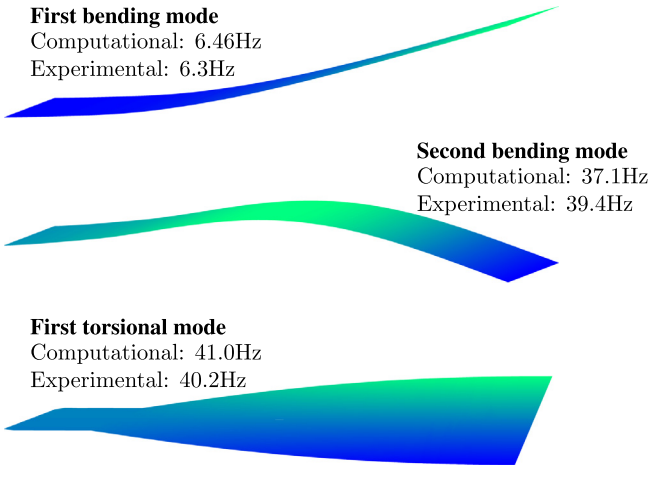

Fig. 6. First three modes of the composite beam.

Feeding the nonlinear model for separated flows into the unsteady state space model of Taha et al. [21], and coupling the developed unsteady nonlinear aerodynamic model with the nonlinear structural model, the aeroelastic behavior of the composite beam was revaluated. Limit cycle oscillations were observed in computational results in the range of wind speeds of the experiments. Fig. 8 shows the output voltage from the piezoelectric layer for two different wind speeds and preset angles. The resistance in this case is $R = 10^6\ \Omega$. A good agreement between experimental and computational results is observed. Some phase difference is observed for the case of $V_\infty = 8$ m/s and $\alpha_0 = 7.2^\circ$, where numerical results predict oscillations with reduced frequency $k = 0.317$ and experimental data show oscillations with reduced frequency $k = 0.262$.

Larger differences in amplitude and phase are identified in Fig. 9 for lower wind speeds. Besides the imprecision during the beam manufacturing, these differences are attributed to the relatively low-fidelity modeling of the aerodynamic characteristics of the beam, at this critical condition during stall; the electric behavior of the output circuit, as well as uncertainties in experimental measurements. In this sense, due to the sensitivity of the system in relation to these effects, small variations in the aerodynamic characteristics or structural features may modify the flutter onset, amplitudes and phases of oscillations in the post-flutter behavior. Moreover, uncertainties in the wind speed measurements also contribute to any unmatching between computational and experimental results. In addition, the computational results for $\alpha_0 = 7.2^\circ$ are in better agreement with the experimental data. Interestingly, this preset angle makes the system to oscillate mostly in the nonlinear aerodynamic regime, as inferred from Fig. 2. Such conclusion reinforces the argument that the use of two states per node may reduce the precision of the computations if the wing is going in and out of the stall regime (i.e., akin to dynamic stall), but it is sufficient when the wing operates in the nonlinear regime. Finally, it should be noted that despite the small discrepancies in some cases, the main picture of the output voltage dynamics is being captured by the computational model. It is worth noticing that the output voltage is the ultimate measurement of the harvest dynamics because it depends on the interaction between structural, aerodynamic, and electrical characteristics of the system. Therefore, the presented results reinforce the model capability on capturing the main features of the energy harvesting from the fluttering beam.

One legitimate question that arises from the result presented in Fig. 8 is the reason why the unsteady model of [21] fed by the nonlinear flow model predicts the post-flutter behavior in agreement with experimental observations, whereas the classical unsteady potential flow theory is not able to indicate the flutter occurrence under the same conditions. To answer this question, the following investigation is conducted in Fig. 10. The aeroelastic response of the beam tip for the case of $V_\infty = 10$ m/s and $\alpha_0 = 5.4^\circ$ (whose voltage output is presented in Fig. 8(b)) is fed to the unsteady model of [21] to compute the circulatory lift using two steady lift characteristics: the potential flow linear model steady lift $2\pi\alpha$ and the Kirchhoff nonlinear model. The lift response (cf Fig. 10(a)) using the nonlinear model is almost constant during the whole excursion while the potential flow model predicts higher and hysteretical forces. On the other hand, the moment coefficient (cf Fig. 10(b)) exhibits a more important difference between both models: while the nonlinear model predicts negative values during the whole motion that decrease as the effective angle of attack increases, the unsteady potential flow theory predicts small val-

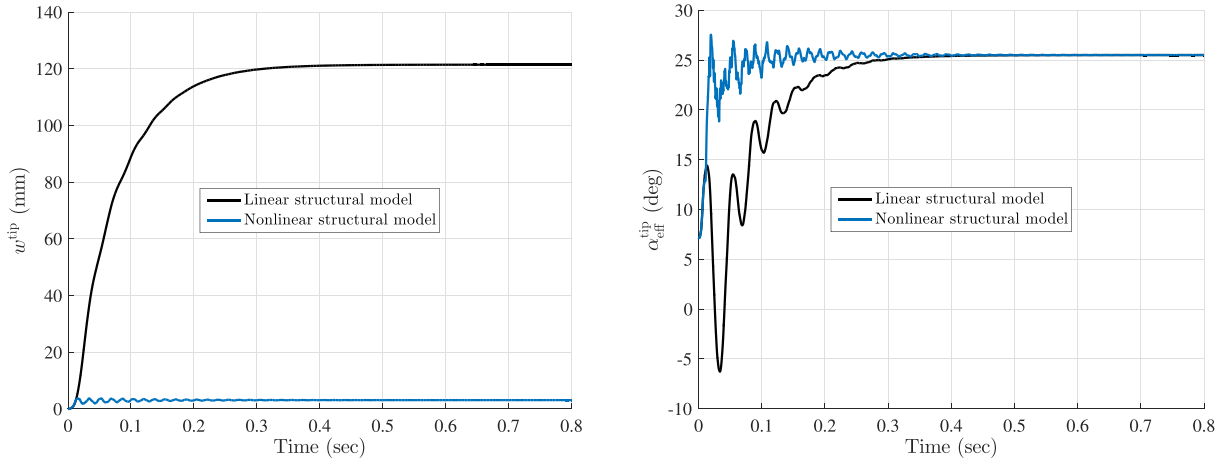

(a) w^{tip} (b) $\alpha_{\text{eff}}^{\text{tip}}$

Fig. 7. Tip displacement and effective angle of attack at $V_\infty = 8$ m/s and $\alpha_0 = 5.4^\circ$ with potential unsteady aerodynamics.

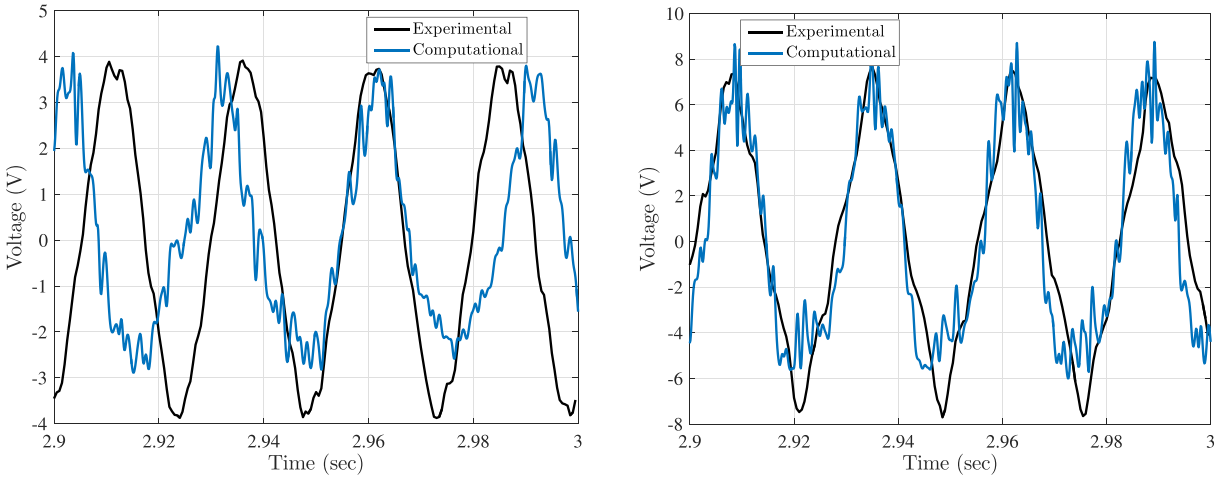

(a) $V_\infty = 8$ m/s and $\alpha_0 = 7.2^\circ$ (b) $V_\infty = 10$ m/s and $\alpha_0 = 5.4^\circ$

Fig. 8. Comparison of the output voltage from experimental and the computational results for different speeds and preset angles.

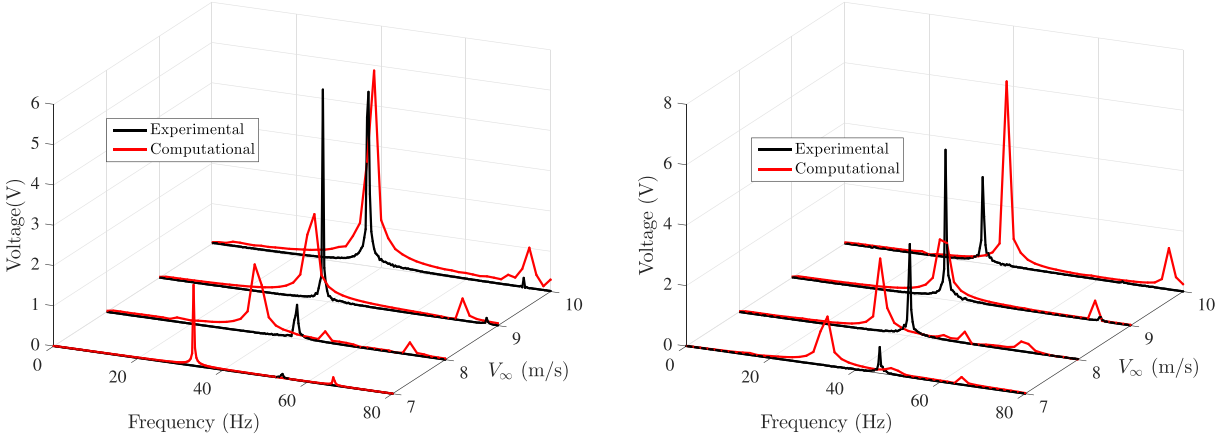

(a) $\alpha_0 = 5.4^\circ$ (b) $\alpha_0 = 7.2^\circ$

Fig. 9. Fast Fourier transform of the output voltage from the simulations and experiments with $R = 10^6$ Ω.

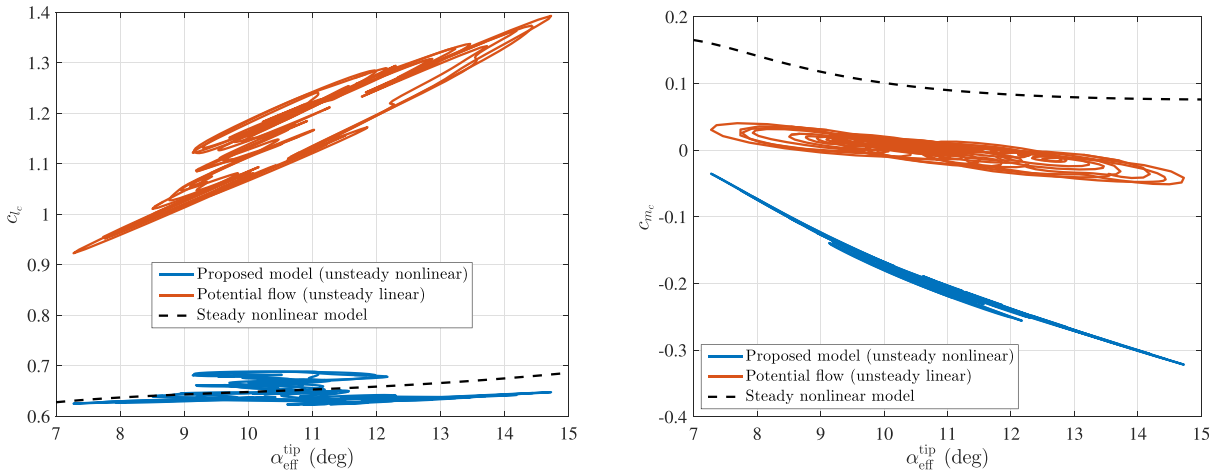

(a) Circulatory lift coefficient (b) Circulatory moment coefficient

Fig. 10. Circulatory loads at the elastic axis for $V_\infty = 10$ m/s and $\alpha_0 = 5.4°$.

ues for the moment coefficient around 0 and even positive. As a consequence, the moment coefficient predicted by the potential model is not able to overcome the structural restoring moment and the flutter onset was still not reached at $V_\infty = 10$ m/s.

6.1. Effects of structural non-linearities

Fig. 7 clearly shows that the linear structural model is not able to predict flutter along with the unsteady potential flow theory. Furthermore, analysis of the post-flutter behavior of the beam in Fig. 8 employed the nonlinear beam model and nonlinear lift characteristics. Therefore, it may be interesting to study the electro-aeroelastic behavior if the nonlinear flow model is applied to the linear structural model. Doing so, the flutter onset was still not observed within the wind speeds of the experimental data ($7 \leqslant V_\infty \leqslant 10$ m/s), although extremely high tip displacements are predicted, which violates the assumption of low displacements for the linear structural model. In conclusion, the use of a nonlinear structural model in the simulation of the electro-aeroelastic behavior of the fluttering beam is crucial for the determination of the flutter boundary. Some other attempts to model the fluttering beam have also been tested but failed to capture the flutter onset observed in experimental results. For example, applying the Kirchhoff correction f to the lift only (*cf* Eq. 10) or to the moment only (*cf* Eq. 12) did not result in a fluttering beam. Table 2 presents a summary of all these approaches by showing when the post-flutter regime is attained within the wind speeds of the experimental data.

7. Conclusions

In this work, the effects of structural and aerodynamic nonlinearities on the modeling of a cantilevered composite beam with a piezoelectric layer intended for energy harvesting purposes are investigated. The experiments conducted have revealed that limit cycle oscillations are achieved in the post-flutter behavior of the beam, and that power can be harvested for wind speeds between 7 and 10 m/s. For the numerical simulations, the Timoshenko beam model is employed for obtaining the governing equations for the structural dynamics of the beam and the piezoelectric lamina, as well as the governing equation for the electric circuit. A finite element method was applied to discretize such equations. The structural model implemented for the beam can assume linear or nolinear strain-displacement relations. On the other hand, unsteady aerodynamics were computed through a state-space model whose input is the quasi-steady circulation to allow for arbitrary nonlinear lift characteristics. The nonlinear aerodynamic effect is represented with the aid of the Kirchhoff model for separated flows. The unsteady potential flow theory was not able to predict flutter within the wind speeds of the experiments, but the unsteady state space model supplied by the Kirchhoff correction coupled with the nonlinear structural model delivered good predictions of the energy harvested in the post-flutter regime of the beam, in comparison to experimental results. Such a difference is mainly due to the moment coefficient predicted by the unsteady nonlinear model, which is negative during the limit cycle oscillations while the moment predicted by the potential theory fluctuates around zero and is sometimes positive, thereby preventing aerodynamic loads from overcoming the restoring structural moment and mitigating the occurrence of flutter. The results presented here, especially the comparison between model and experiment, have demonstrated that an appropriate modeling of both flow and structural dynamics is crucial in order to accurately describe the complex physics involved in the phenomenon. Future developments include a nonlinear kinematic description of the beam displacements in order to account for large rotations.

8. Data availability

The raw data required to reproduce these findings are available to download from Mendeley Data.

Table 2
Summary of the methods employed in this work.

	Potential flow	Nonlinear model (lift only)	Nonlinear model (moment only)	Nonlinear model (lift & moment)
Linear beam	No flutter	No flutter	No flutter	No flutter
Nonlinear beam	No flutter	No flutter	No flutter	Flutter

CRediT authorship contribution statement

Carlos R. dos Santos: Conceptualization, Methodology, Software, Validation, Writing - original draft. **Douglas R. Q. Pacheco:** Conceptualization, Methodology, Software, Validation, Writing - original draft. **Haithem E. Taha:** Conceptualization, Methodology, Writing - review & editing. **Mohamed Y. Zakaria:** Conceptualization, Validation, Investigation, Writing - review & editing.

Declaration of Competing Interest

The authors declare that they have no known competing financial interests or personal relationships that could have appeared to influence the work reported in this paper.

Acknowledgments

The first author acknowledge the sponsorship of the Brazilian agency: grants #2017/09468-6 and #2018/05247-8, São Paulo Research Foundation (FAPESP). The last author acknowledges the support of the NSF Grant CMMI-1846308.

References

[1] Lee BHK, Price SJ, Wong YS. Nonlinear aeroelastic analysis of airfoils: bifurcation and chaos. Prog Aerosp Sci 1999;35(3):205–334. https://doi.org/10.1016/S0376-0421(98)00015-3.
[2] Patil MJ, Hodges DH. On the importance of aerodynamic and structural geometrical nonlinearities in aeroelastic behavior of high-aspect-ratio wings. J Fluids Struct 2004;19(7):905–15. https://doi.org/10.1016/j.jfluidstructs.2004.04.012.
[3] Zakaria MY, Eliethy AS, Canfield RA, Hajj MR. A novel imaging technique for measuring kinematics of light-weight flexible structures. Rev Sci Instrum 2016;87(7):. https://doi.org/10.1063/1.4955442075108.
[4] Al-Haik MY, Boroujeni AY, Zakaria MY, Hajj MR. Effect of embedding ZnO nanorods on nonlinear response of composite beams. Nonlinear Dyn 2017;90(2):1179–89. https://doi.org/10.1007/s11071-017-3719-3.
[5] Modaress-Aval AH, Bakhtiari-Nejad F, Dowell EH, Peters DA, Shahverdi H. A comparative study of nonlinear aeroelastic models for high aspect ratio wings. J Fluids Struct 2019;85:249–74. https://doi.org/10.1016/j.jfluidstructs.2019.01.003.
[6] Abdelkefi A. Aeroelastic energy harvesting: A review. Int J Eng Sci 2016;100:112–35. https://doi.org/10.1016/j.ijengsci.2015.10.006.
[7] Al-Haik MY, Zakaria MY, Hajj MR, Haik Y. Storage of energy harvested from a miniature turbine in a novel organic capacitor. J Energy Storage 2016;6:232–8. https://doi.org/10.1016/j.est.2016.01.008.
[8] Liu D, Al-Haik M, Zakaria M, Hajj MR. Piezoelectric energy harvesting using L-shaped structures. J Intell Mater Syst Struct 2018;29(6):1206–15. https://doi.org/10.1177/1045389X17730926.
[9] Marques FD, Pereira DA, Zakaria MY, Hajj MR. Power extraction from stall-induced oscillations of an airfoil. J Intell Mater Syst Struct 2018;29(7):1407–17. https://doi.org/10.1177/1045389X17739161.
[10] Hémon P, Amandolese X, Andrianne T. Energy harvesting from galloping of prisms: A wind tunnel experiment. J Fluids Struct 2017;70:390–402. https://doi.org/10.1016/j.jfluidstructs.2017.02.006.
[11] Franzini GR, Bunzel LO. A numerical investigation on piezoelectric energy harvesting from vortex-induced vibrations with one and two degrees of freedom. J Fluids Struct 2018;77:196–212. https://doi.org/10.1016/j.jfluidstructs.2017.12.007.
[12] Tang DM, Dowell EH. Aeroelastic response and energy harvesting from a cantilevered piezoelectric laminated plate. J Fluids Struct 2018;76:14–36. https://doi.org/10.1016/j.jfluidstructs.2017.09.007.
[13] Zakaria MY, Al-Haik MY, Hajj MR. Experimental analysis of energy harvesting from self-induced flutter of a composite beam. Appl Phys Lett 2015;107(2):. https://doi.org/10.1063/1.4926876023901.
[14] Amini Y, Emdad H, Farid M. An accurate model for numerical prediction of piezoelectric energy harvesting from fluid structure interaction problems. Smart Mater Struct 2014;23(9):. https://doi.org/10.1088/0964-1726/23/9/095034095034.
[15] Zhao MH, Zhang W. Nonlinear dynamics of composite laminated cantilever rectangular plate subject to third-order piston aerodynamics. Acta Mech 2014;225(7):1985–2004. https://doi.org/10.1007/s00707-013-1035-7.
[16] Hao YX, Niu Y, Zhang W, Li SB, Yao MH, Wang AW. Supersonic flutter analysis of FGM shallow conical panel accounting for thermal effects. Meccanica 2018;53(1–2):95–109. https://doi.org/10.1007/s11012-017-0715-0.
[17] Lu SF, Zhang W, Song XJ. Time-varying nonlinear dynamics of a deploying piezoelectric laminated composite plate under aerodynamic force. Acta Mech Sin 2018;34(2):303–14. https://doi.org/10.1007/s10409-017-0705-4.
[18] Dunnmon JA, Stanton SC, Mann BP, Dowell EH. Power extraction from aeroelastic limit cycle oscillations. J Fluids Struct 2011;27(8):1182–98. https://doi.org/10.1016/j.jfluidstructs.2011.02.003.
[19] De Marqui Jr C, Tan D, Erturk A. On the electrode segmentation for piezoelectric energy harvesting from nonlinear limit cycle oscillations in axial flow. J Fluids Struct 2018;82:492–504. https://doi.org/10.1016/j.jfluidstructs.2018.07.020.
[20] Thwaites B. Incompressible Aerodynamics. Oxford, United Kingdom: Oxford University Press; 1960.
[21] Taha HE, Hajj MR, Beran PS. State-space representation of the unsteady aerodynamics of flapping flight. AerospSci Technol 2014;34:1–11. https://doi.org/10.1016/j.ast.2014.01.011.
[22] Abbas MK, Elshafei MA, Negm HM. Modeling and analysis of laminated shape memory alloy composite plates. JThermoplast Compos Mater 2016;29(1):103–42. https://doi.org/10.1177/0892705715599432.
[23] Karamanlí A. Flexure analysis of laminated composite and sandwich beams using Timoshenko beam theory. Politeknik Dergisi 2018;21(3):633–43. https://doi.org/10.2339/politeknik.386958.
[24] Dietl JM, Garcia E. Beam shape optimization for power harvesting. J Intell Mater Syst Struct 2010;21(6):633–46. https://doi.org/10.1177/1045389X10365094.
[25] Theodorsen T. General theory of aerodynamic instability and the mechanism of flutter, Tech. Rep. TR-496, NACA; 1935.
[26] Zakaria MY, Taha HE, Hajj MR, Hussein AA. Experimental-based unified unsteady nonlinear aerodynamic modeling for two-dimensional airfoils. In: 33rd AIAA applied aerodynamics conference. p. 3167. https://doi.org/10.2514/6.2015-3167.
[27] Zakaria MY, Taha HE, Hajj MR. Measurement and modeling of lift enhancement on plunging airfoils: A frequency response approach. J Fluids Struct 2017;69:187–208. https://doi.org/10.1016/j.jfluidstructs.2016.12.004.
[28] Leishman JG, Beddoes TS. A generalised model for airfoil unsteady aerodynamic behaviour and dynamic stall using the indicial method. In: 42nd annual forum of the american helicopter society, Washington DC. p. 243–65.
[29] Leishman JG, Crouse Jr GL. State-space model for unsteady airfoil behavior and dynamic stall. In: 30th Structures, structural dynamics and materials conference; 1989. p. 1372–83. doi:10.2514/6.1989-1319.
[30] Leishman JG, Nguyen KQ. State-space representation of unsteady airfoil behavior. AIAA J 1990;28(5):836–44. https://doi.org/10.2514/3.25127.
[31] van der Wall BG, Leishman JG. On the influence of time-varying flow velocity on unsteady aerodynamics. J Am Helicopter Soc 1994;39(4):25–36. https://doi.org/10.4050/JAHS.39.25.
[32] von Kármán T, Sears WR. Airfoil theory for non-uniform motion. J Aeronaut Sci 1938;5(10):379–90. https://doi.org/10.2514/8.674.
[33] Jones RT. Operational treatment of the nonuniform-lift theory in airplane dynamics, Tech. Rep. TR-667, NACA; 1938.
[34] Yan Z, Taha HE, Hajj MR. Geometrically-exact unsteady model for airfoils undergoing large amplitude maneuvers. Aerosp Sci Technol 2014;39:293–306. https://doi.org/10.1016/j.ast.2014.09.021.
[35] Bisplinghoff RL, Ashley H, Halfman RL. Aeroelasticity. Massachusetts: Addison-Wesley; 1957.
[36] Kirchhoff G. Zur Theorie freier Flüssigkeitsstrahlen. J für die Reine und Angew Math 1869;70:289–98. https://doi.org/10.1515/crll.1869.70.289.
[37] Wang ZJ, Birch JM, Dickinson MH. Unsteady forces and flows in low Reynolds number hovering flight: two-dimensional computations vs robotic wing experiments. J Exp Biol 2004;207(3):449–60. https://doi.org/10.1242/jeb.00739.
[38] Leishman JG, Beddoes TS. A semi-empirical model for dynamic stall. J Am Helicopter Soc 1989;34(3):3–17. https://doi.org/10.4050/JAHS.34.3.3.
[39] Okamoto M, Yasuda K, Azuma A. Aerodynamic characteristics of the wings and body of a dragonfly. J Exp Biol 1996;199(2):281–94.
[40] Amandolese X, Michelin S, Choquel M. Low speed flutter and limit cycle oscillations of a two-degree-of-freedom flat plate in a wind tunnel. J Fluids Struct 2013;43:244–55. https://doi.org/10.1016/j.jfluidstructs.2013.09.002.
[41] Pacheco DRQ, Ferreira AJM, Marques FD. On the effects of structural coupling on the supersonic flutter and limit cycle oscillations of transversely reinforced panels. J Fluids Struct 2018;79:158–70. https://doi.org/10.1016/j.jfluidstructs.2018.01.013.
[42] Lee D-M, Lee I. Vibration analysis of anisotropic plates with eccentric stiffeners. Comput Struct 1995;57(1):99–105. https://doi.org/10.1016/0045-7949(94)00593-R.
[43] Rosa M, De Marqui Jr C. Modeling and analysis of a piezoelectric energy harvester with varying cross-sectional area. Shock Vib 2014. https://doi.org/10.1155/2014/930503.
[44] Pacheco DRQ, Marques FD, Ferreira AJM. Finite element analysis of fluttering plates reinforced by flexible beams: An energy-based approach. J Sound Vib 2018;435:135–48. https://doi.org/10.1016/j.jsv.2018.07.042.
[45] Henry CJ. Hydrofoil flutter phenomenon and airfoil flutter theory, Tech. rep., Davidson Laboratory; 1961.
[46] Abramson HN, Ransleben GE. An experimental investigation of flutter of a fully submerged subcavitating hydrofoil. J Aircr 1965;2(5):439–42. https://doi.org/10.2514/3.43681.
[47] Taha H, Rezaei AS. Viscous extension of potential-flow unsteady aerodynamics: the lift frequency response problem. J Fluid Mech 2019;868:141–75. https://doi.org/10.1017/jfm.2019.159.